Scripta Materialia 249 (2024) 116177

Contents lists available at ScienceDirect

Scripta Materialia

journal homepage: www.journals.elsevier.com/scripta-materialia

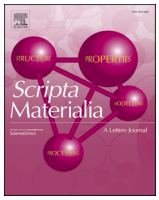

Microstructure and phase evolution of Fe-20Ni-20W foams during high-temperature redox cycling

Samuel Pennell *, David C. Dunand

Northwestern University, Evanston, IL 60208, USA

ARTICLE INFO

Keywords:
Redox cycling
Freeze casting
Energy storage
Porosity
Metals and alloys

ABSTRACT

Freeze-cast Fe-20Ni-20 W (at%) foams suitable for high-temperature redox cycling show excellent microstructural stability and regenerative porosity formation, but they exhibit slower reduction kinetics as compared to previously studied Fe-25 W foams. The Fe-20Ni-20 W lamellar foams, after initial hydrogen reduction, consist of a two-phase mixture of μ-Fe_7W_6 and γ-Fe(Ni,W), with significant microporosity due to the sintering inhibition of W. During oxidation by steam at 800 °C, these phases are oxidized to a three-phase mixture of (Fe,Ni)WO_4, Fe_3O_4, and γ-Ni(Fe); upon subsequent reduction by H_2, the foams return to their initial composition. The chemical vapor transport reduction of $FeWO_4$ results in the formation of submicron pores during each reduction half-cycle which accelerate subsequent reaction and limit sintering in the reduced state. The reduction of mixed oxide is relatively sluggish, which is likely due to the increased stability of the (Fe,Ni)WO_4 phase brought on by the substitution of Ni in Fe sites in $FeWO_4$.

Introduction

Iron powders are attractive for redox-based energy storage devices operating at high temperature, such as rechargeable oxide batteries (ROB) or cyclic looping combustion reactors (CLC), due to their low cost, low toxicity, and high reactivity in both oxidizing and reducing environments [1–5]. However, the development of these technologies has been stunted by rapid degradation of Fe powder beds during redox cycling at high temperatures [6,7]. Due to the large volumetric expansion of Fe during oxidation, neighboring particles substantially increase their contact area in the oxidized state. Then, due to the high temperature of operation, contacting particles irreversibly sinter, reducing the surface area of the particle system. In just a few redox cycles, this sintering and densification mechanism degrades drastically any initially high reactivity. Two strategies have been researched to minimize this sintering-induced degradation: (i) utilizing additives that, when mixed with Fe, can mitigate degradation on a microstructural level [8,9], (ii) structured fabrication techniques (e.g., directional freeze casting [10]) designed to create porous architectures that will mitigate densification on a macrostructural level.

Previously, we have shown the efficacy of tungsten as a sintering inhibition agent when alloyed with iron [11]. Due to the very high melting point of W, its ability to undergo redox reactions, and its unique chemical vapor transport (CVT) reduction mechanism, Fe-25 W foams show excellent stability (i.e., no sintering) over 100 full redox cycles [11]. Additionally, we have previously shown that nickel is effective in accelerating the reduction kinetics of Fe_3O_4 and FeO to Fe at high temperatures [12]. Both studies utilized directionally freeze-cast foams with thin lamellae (10–20 μm wide), to ensure gas access and minimal degradation. Since the main drawback observed in the Fe-25 W study is a long reduction period, we hypothesize here that Ni additions accelerates reduction, improving the performance of the Fe-W system.

Here, we present the high-temperature redox cycling behavior of Fe-20Ni-20 W (at%) freeze-cast foams. This composition was chosen to ensure both high W content for sintering inhibition, and high Ni content to accelerate reduction. As described in detail below, we find that, while the foams retain the excellent redox stability expected from the high W content, the Ni addition does not accelerate reduction, while also slowing oxidation. This unexpected lack of effect from Ni is attributed to the formation of ternary Fe-W-Ni-based oxides with high stability.

Fe-20Ni-20 W (at.%) lamellar foams were fabricated by preparing an aqueous (87.5 vol% H_2O) slurry composed of oxide powders – 5.11 vol% Fe_2O_3 (Noah Technologies, 99.9 %, < 3 μm), 1.25 vol% NiO (Skyspring nano, 99.9 %, 50 nm), and 3.63 vol% WO_3 (Skyspring nano, 99.5 %, < 100 nm) - in the correct proportion to form the desired final composition after reduction; micrographs of the oxide powders are shown in

* Corresponding author.
E-mail address: samuelpennell2024@u.northwestern.edu (S. Pennell).

https://doi.org/10.1016/j.scriptamat.2024.116177
Received 4 March 2024; Received in revised form 4 May 2024; Accepted 14 May 2024
Available online 17 May 2024

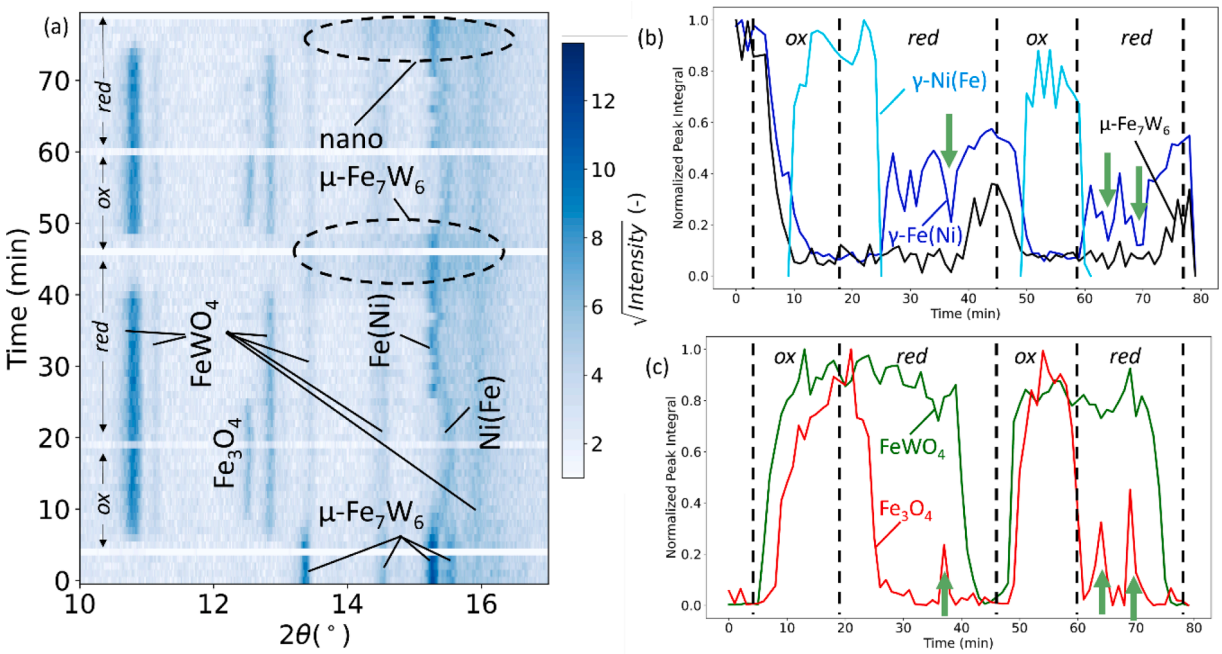

Fig. 1. In situ X-Ray diffraction data for redox cycling of Fe-20Ni-20 W lamellae at 800 °C. (a) Waterfall XRD spectra are shown as a function of time for the first two redox cycles, with all phases labelled. (b) Normalized peak integrals for metallic phases: μ-Fe_7W_6 (black), γ-Fe(Ni) (dark blue), and γ-Ni(Fe) (cyan). The two γ phases are distinguished by their peak positions, with the Ni-rich γ-Ni(Fe) peak shifted to higher 2θ values as compared to the Fe-rich γ-Fe(Ni) peak; for this reason, the γ-Ni (Fe) signal is only analyzed when at a 2θ value distinct from the γ-Fe(Ni). (c) Normalized peak integrals for oxide phases: $FeWO_4$ (green) and Fe_3O_4 (red). Green arrows in (b,c) mark instances of transient re-oxidation during the reduction half-cycles.

Supplementary Figure 1. 0.5 vol% Zephrym PD4974 (Croda) was used as a dispersant to prevent agglomeration of the oxide particles. The slurry was ball milled with yttrium-stabilized zirconia milling media for 24 h to ensure good mixing of the powders, then combined with the polymer binder (2 vol% polyethylene glycol (M_n=3350, Sigma Aldrich)), directionally freeze-cast, freeze-dried, debinded, and reduced under H_2 according to previously reported details [11]. Redox cycling was performed at 800 °C - under flowing H_2O for oxidization, and under flowing H_2 for reduction - with details reported in Ref. [11] In-situ X-ray diffraction (XRD) during redox cycling was performed on a small portion of a foam under conditions similar to the bulk redox cycling. Following a ramp at 30 °C/min to 800 °C, data were acquired in 1-minute spectra until the experiment was completed. Unlike previous studies which used Ar-4 %H_2 as the reducing gas, pure H_2 was used for our in situ experiment, because of the increased thermodynamical stability of the oxidized state as discussed below. Microstructural characterization (SEM) used the same techniques as reported in Ref. [11].

In situ XRD results for Fe-20Ni-20 W freeze cast foams are shown in Fig. 1 for reduction at 800 °C by pure H_2 and oxidation by steam with Ar as a carrier gas.

Fig. 1a shows time-resolved XRD spectra for the first two redox cycles. The corresponding normalized peak integrals for the strongest peak of each phase are shown for the metallic phases (Fig. 1b) and for the oxide phases (Fig. 1c). The four blanks in the data are times when diffraction spectra were not measured while the gas environment was changed, corresponding to the change between a reducing environment (abbreviated *red*) and an oxidizing environment (abbreviated *ox*). The expected equilibrium phase composition in the reduced state at 800 °C is shown in the ternary phase diagram in Supplementary Figure 2.

The foam initially consists of a two-phase mixture of μ-Fe_7W_6 and γ-Fe(Ni), after reduction at 1200 °C from the freeze-cast oxides. As shown in Fig. 1(a-c), oxidation begins at $t = 5$ min, immediately upon H_2O (steam) exposure and proceeds rapidly, such that the formation of the transient FeO phase is not resolved at the scan time of 1 min. $FeWO_4$ first forms 2 min into oxidation, with subsequent, slower formation of Fe_3O_4 at 5 min into oxidation. The formation of Fe_3O_4 is accompanied by a shift in the lattice parameter of the γ-Ni solid solution (to higher value, for the peak at 2θ=15.6°), as Fe in the matrix is oxidized and Ni becomes the majority element. The Fe-Ni-O phase diagram indicates that, at full oxidation, the γ-Ni(Fe) solid solution contains ~12 % Fe. At $t = 19$ min, the gases are switched and reduction under H_2 begins. Fe_3O_4 is reduced first, in 6 min, with a corresponding return of the γ-Ni lattice parameter to its initial state. Reduction of $FeWO_4$ takes a much longer time (23 min), forming nano-crystalline Fe_7W_6, resulting in broad, poorly resolved peaks rather than the initially sharp peaks observed for $t < 5$ min (before the start of oxidation). These nanocrystals influence successive cycles, as shown by the second oxidation and reduction: both are accelerated, with oxidation completed in 10 min, and reduction completed in 17 min. The transient re-formation of Fe_3O_4 during the reduction period (as seen by data at $t = 35$, 65, and 70 min) indicates that there may be some gas flow tortuosity, resulting in evolved steam re-oxidizing previously reduced portions of the sample.

The acceleration of reaction kinetics after the first redox cycle is consistent with previous studies of Fe-25 W and Fe-25Mo lamellar foams [11,13]. It is attributed to an increase in surface area and decrease in diffusion distance associated with the formation of nanocrystalline intermetallic phases and corresponding submicron porosity. While this is also observed for Fe-20Ni-20 W, the overall reduction rate is much slower than expected for reduction with pure H_2. For comparison, reduction of Fe-25 W under pure H_2 takes 15 min for the first cycle, and 7 min for the second cycle (shown in Supplementary Figure 3), compared to present results (23 and 17 min for Fe-20Ni-20 W, respectively). This result is unexpected, given the reduction acceleration effect as compared to pure Fe observed in the Fe-25Ni binary system [12]. This slowdown in reduction is attributed to increased stability of the mixed oxide $FeWO_4$. While a distinct $Fe_xNi_yWO_z$ compound is not formed, substitution of Ni into the Fe sites of $FeWO_4$ is likely (forming (Fe,Ni)WO_4), and a similar substitution is observed in the intermetallic Fe_7W_6 (forming $(Fe,Ni)_7W_6$). This Ni substitution is expected to increase the stability of the mixed oxide via configurational entropy, and it appears

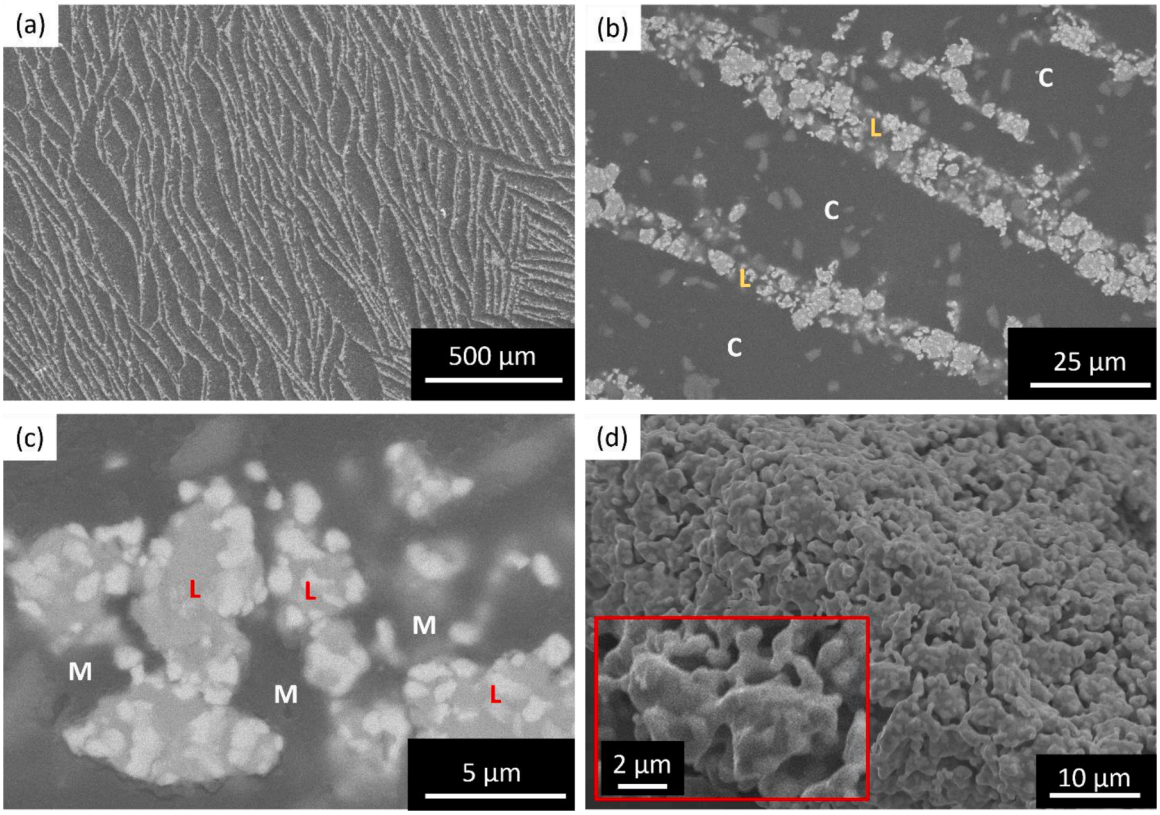

Fig. 2. Micrographs of Fe-20Ni-20 W freeze-cast foams after reduction and sintering. (a) radial cross-section electron image showing a macroscopic view of lamellae and channels, (b) radial cross-section electron image of channels (letter C) and lamellae (yellow letter L) (c) higher magnification electron image of lamella interior (radial foam cross-section) with ligaments (red letter L) and micropores (letter M) showing a two-phase microstructure (μ-Fe_7W_6 (white) and γ-Fe(Ni,W) (dark gray)), and (d) electron image of the surface of an unmounted lamella, showing microporous network made possible by sintering inhibition, with ligaments exhibiting a two-phase microstructure, shown in inset.

to be sufficient to negate any gains in reduction kinetics compared to the binary Fe_3O_4 reduction.

Microstructurally, the Fe-20Ni-20 W foams closely resemble previously studied Fe-25 W foams. After freeze-casting and reduction of the blends of oxide powder followed by sintering at 1200 °C, the microstructure consists of a fully densified, interpenetrating network of γ-Fe (Ni) and μ-Fe_7W_6. Based on the ternary Fe-Ni-W phase diagram in Supplementary Figure 2, an equimolar mixture of γ-Fe(Ni,W) and μ-(Fe, Ni)7W6 is expected, and this phase mixture is observed in the as-fabricated foams. Both phases contain a high amount of Fe, the difference in the observed size is a result of the difference in sintering and coarsening behavior. The γ-Fe(Ni,W) contains relatively little W, and

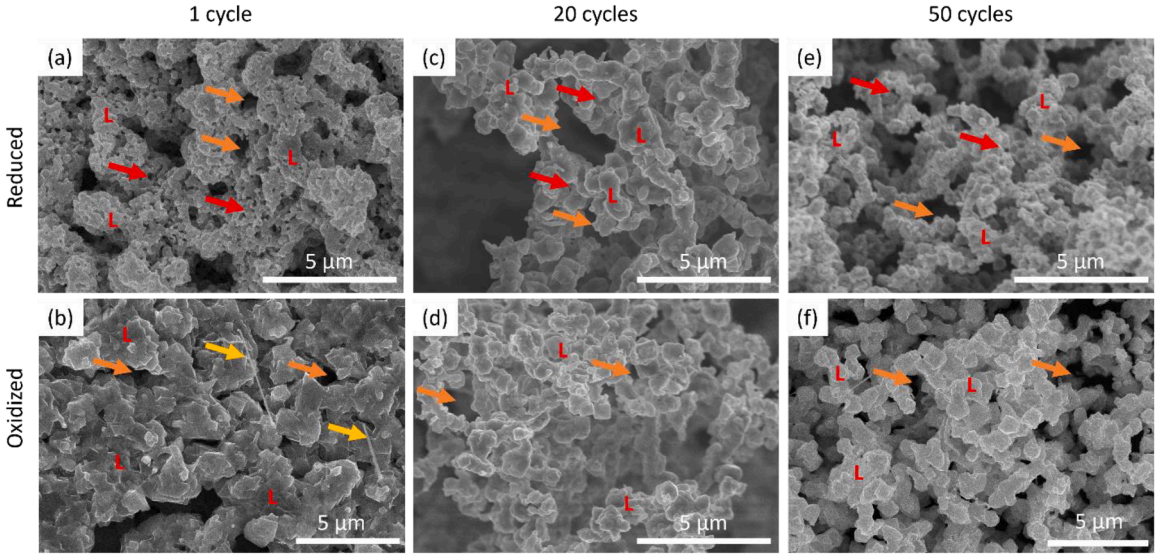

Fig. 3. Electron micrographs showing surface structure of a single Fe-20Ni-20 W lamella after 1, 20, and 50 cycles in the reduced (top row) and oxidized (bottom row) states. Orange arrows mark micropores, red arrows mark submicron pores, red letter L marks examples of ligaments, and yellow arrows mark $FeWO_4$ whiskers.

will thus coarsen and sinter much more than the intermetallic phase with high W content. Because of this, the γ-Fe(Ni,W) regions are larger. This initial state is shown in Fig. 2 at three different magnifications. The overall foam architecture, shown from a radial cross-section in Fig. 2a consists of metallic lamellae with uniform thickness separated by channels with varying width depending on the deformation of the neighboring lamellae. Fig. 2b shows a polished radial cross section of a group of lamellae (yellow letter L), each between 10 and 20 μm in thickness, separated by channels (letter C) templated by ice during the freeze casting step. The lamellae have significant internal porosity, as shown in Fig. 2c. The lamellar microstructure consists of an interpenetrating network of solid ligaments (red letter L) and micropores (letter M). The solid ligaments are composed of μ-Fe_7W_6 (white) and γ-Fe(Ni,W) (dark gray). Both phases are present in ligaments <10 μm in size. The high volume fraction of both phases indicates that they are interpenetrating. Fig. 2d shows a single, unmounted lamella after reduction and sintering. The same two-phase network is visible, and the presence of significant microporosity is observed as well, forming an interconnected 3-dimensional porous network. This porosity remains from the volume contraction associated with the reduction of the green body oxide powders, and it does not sinter due to the sintering inhibition of the μ-Fe_7W_6 phase.

Because of the sintering inhibition effects of W, the lamellae are initially porous, and they become increasingly porous with cycling. The overall utilization of Fe in each foam was determined by comparing the mass of the foam before cycling, after oxidation, and after reduction. All foams were able to fully oxidize and reduce in each 90-miunte oxidation and 90-minute reduction period, up to the measured 50 cycles. Microstructural characterization did not reveal any directionality with respect to the foam reaction (e.g., residual oxidation at the top of the foam). The microstructure of a single lamella for foams subjected to 1, 20, and 50 cycles, in the reduced and oxidized states, is shown in Fig. 3. The in situ XRD results (Fig. 1) indicate the formation of nanocrystalline μ-Fe_7W_6 after the first oxidation/reduction cycle. This reduced state is shown in Fig. 3a. The microporosity present within each lamella is significantly increased: the microporous network (orange arrows) expands in volume, and submicron pores (red arrows) are visible between metallic ligaments (red letter L) comprising the lamella. The micropores probably expand due to gas egress: on reduction, steam is produced at free surfaces around each open micropore with gas access and it escapes through the microporous network, causing the pores to expand; this process has been observed in other redox cycling studies as well [12]. Because the μ-Fe_7W_6 phase is a strong sintering inhibitor, the newly-created and expanded micropores do not disappear by sintering after each cycle; this leads to a progressive increase in the porosity of the lamellae with continued cycling. The submicron pores form due to the reduction mechanism of $FeWO_4$: this phase reduces in the presence of H_2 by chemical vapor transport (CVT) forming a transient hydrated vapor phase ($WO_3(OH)_2$) which further reacts with H_2 to condense as W on the surrounding Fe free surfaces with gas access, then reacts to form μ-Fe_7W_6 [14–16]. This gas-phase-precipitated μ phase is nanocrystalline, as indicated by the XRD results, with submicron pores separating neighboring nanocrystalline μ-phase grains. Like the micropores, these submicron pores do not sinter due to the high sintering inhibition of the μ phase that borders them. In the oxidized state after 1 cycle (Fig. 3b), the microporous network remains present (orange arrows), though it is somewhat filled because of the volumetric as the metallic phase oxidizes to $FeWO_4$ and Fe_3O_4. Formation of $FeWO_4$ whiskers (yellow arrows) is observed as well.

After 20 cycles in the reduced state (Fig. 3c), the microporous network has expanded further, with each lamella more closely resembling a fully porous powder foam rather than a sintered platelet. The cyclic redistribution of W during each reduction cycle shrinks the size of the γ and μ phases, with each becoming approximately micron-sized. Submicron pores are prevalent throughout these micron size phases. The oxidized state (Fig. 3d) closely resembled the reduced state, with individual Fe_3O_4 and $FeWO_4$ particles observed on the lamellar surface. After 50 cycles, the microstructure has not changed, with similar pore and particle size in the reduced (Fig. 3e) and oxidized (Fig. 3f) states. Throughout cycling, the metallic Ni(Fe) phase which does not oxidize remains well-distributed throughout the microstructure.

In conclusion, Fe-20Ni-20 W lamellar foams are resistant against degradation upon long-term redox cycling, with no sintering or elemental segregation observed after 50 cycles. The lamellae, which are not fully dense initially, grow progressively more porous with cycling due to the CVT mechanism, and the size of each phase decreases from ~5 μm in the as-fabricated state to micron or submicron after 20 cycles, with no significant change observed between 20 and 50 cycles. The metallic Ni phase does not provide a strong accelerating effect on the reduction process, making its addition unnecessary in view of similar microstructural results obtained for binary Fe-25 W lamellar foams fabricated via the same freeze-casting process. The lack of improvement in reduction kinetics can be explained by (i) the CVT reduction mechanism of $FeWO_4$, which does not benefit from the presence of Ni, and (ii) the formation of more stable quaternary (Fe,Ni)WO_4 oxides due to the presence of Ni, which are slower to reduce than ternary $FeWO_4$. Thus, while Fe_3O_4 reduces rapidly, the overall rate of reduction of the entire phase system does not benefit from the presence of Ni, due to the formation of this more stable oxide phase.

CRediT authorship contribution statement

Samuel Pennell: Conceptualization, Investigation, Methodology, Visualization, Writing – original draft, Writing – review & editing. **David C. Dunand:** Conceptualization, Funding acquisition, Project administration, Supervision, Visualization, Writing – review & editing.

Declaration of competing interest

The authors declare the following financial interests/personal relationships which may be considered as potential competing interests:

DCD discloses a financial interest in CellMobility, Inc. which commercializes freeze-cast metal foams. DCD and SMP disclose patent applications for "Refractory Alloyed Iron-based redox active foams for Iron-Air Batteries", U.S. Provisional Patent Application No. 63/406,320 and “Iron-Tungsten Redox System and Applications of Same”, U.S. Provisional Patent Application No. 63/619.401.

Acknowledgments

This research was funded by the US National Science Foundation under grant CMMI-2015641. Experiments and characterization made use of the Materials Characterization and Imaging Facility, the NUANCE Center (supported by SHyNE under NSF ECCS-1542205, MRSEC under NSF DMR-1720139, the International Institute for Nanotechnology, the Keck Foundation, and the State of Illinois), and the IMSERC X-Ray facility (supported by SHyNE under NSF ECCS-2025633) at Northwestern University (NU). The authors thank Dr. Ming Chen for useful discussions.

Supplementary materials

Supplementary material associated with this article can be found, in the online version, at doi:10.1016/j.scriptamat.2024.116177.

References

[1] X. Zhao, Y.H. Gong, X. Li, N.S. Xu, K. Huang, Research progress of a new solid oxide metal-air redox battery for advanced energy storage, Mater. Sci. Forum 783-786 (2014) 1667–1673.

[2] P. Gayán, M.A. Pans, M. Ortiz, A. Abad, L.F. de Diego, F. García-Labiano, J. Adánez, Testing of a highly reactive impregnated Fe2O3/Al2O3 oxygen carrier

for a SR–CLC system in a continuous CLC unit, Fuel Process. Technol. 96 (2012) 37–47.
[3] N. Xu, X. Li, X. Zhao, J.B. Goodenough, K. Huang, A novel solid oxide redox flow battery for grid energy storage, Energy Environ. Sci. 4 (12) (2011) 4942–4946.
[4] R.D. McKerracher, C.P. de Leon, R.G.A. Wills, A.A. Shah, F.C. Walsh, A review of the iron-air secondary battery for energy storage, Chempluschem 80 (2) (2015) 323. -+.
[5] X. Han, L. Wang, Z. Ge, X. Lin, Y. Liu, S. Zhang, Z. Zuo, H. Chen, Al- and Cr-doped Co_3O_4/CoO redox materials for thermochemical energy storage in concentrated solar power plants, Sol. Energy Mater. Sol. Cells 260 (2023) 112475.
[6] C.D. Bohn, J.P. Cleeton, C.R. Müller, S.Y. Chuang, S.A. Scott, J.S. Dennis, Stabilizing iron oxide used in cycles of reduction and oxidation for hydrogen production, Energy Fuels 24 (7) (2010) 4025–4033.
[7] T. Mattisson, M. Johansson, A. Lyngfelt, Multicycle reduction and oxidation of different types of iron oxide particles application to chemical-looping combustion, Energy Fuels 18 (3) (2004) 628–637.
[8] K. Otsuka, T. Kaburagi, C. Yamada, S. Takenaka, Chemical storage of hydrogen by modified iron oxides, J. Power Sources 122 (2) (2003) 111–121.
[9] B. Jin, N.V. Srinath, H. Poelman, C. Detavernier, Z. Liang, G.B. Marin, V.V. Galvita, Separate H_2 and CO production from CH_4-CO_2 cycling of Fe-Ni, AlChE J. 68 (9) (2022) e17779.
[10] M. Damizia, P.J. Lloreda-Jurado, P. De Filippis, B. de Caprariis, E. Chicardi, R. Sepúlveda, Green hydrogen production using doped Fe_2O_3 foams, Int. J. Hydrogen Energy 51 (2024) 834–845.
[11] S. Pennell, M. Chen, D.C. Dunand, Tungsten strongly inhibits sintering of porous iron during high-temperature redox cycling, Small (2024).
[12] J.B. Mack, S.M. Pennell, D.C. Dunand, Microstructural evolution of lamellar Fe-25Ni foams during steam-hydrogen redox cycling, Acta Mater. 237 (2022) 118148.
[13] J.B. Mack, S.M. Pennell, D.C. Dunand, Sintering inhibition enables hierarchical porosity with extreme resistance to degradation during redox cycling of Fe-Mo foams, Acta Mater. (2023) 119015.
[14] X.-W. Wu, J.-S. Luo, B.-Z. Lu, C.-H. Xie, Z.-M. Pi, M.-Z. Hu, T. XU, G.-G. Wu, Z.-M. Yu, D.-Q. Yi, Crystal growth of tungsten during hydrogen reduction of tungsten oxide at high temperature, Trans. Nonferrous Metals Soc. China 19 (2009) s785–s789.
[15] W. Schubert, Kinetics of the hydrogen reduction of tungsten oxides, Int. J. Refractory Hard Metals 9 (4) (1990) 178–191.
[16] W. Schubert, E. Lassner, Production and characterization of hydrogen-reduced submicron tungsten powders—Part 1: state of the art in research, production and characterization of raw materials and tungsten powders, Int. J. Refract. Met. Hard Mater. 10 (3) (1991) 133–141.